IOP Publishing Phys. Med. Biol. 65 (2020) 035008 (12pp) https://doi.org/10.1088/1361-6560/ab6578

Physics in Medicine & Biology

IPEM Institute of Physics and Engineering in Medicine

PAPER

Quantitative analysis of a micro array anode structured target for hard x-ray grating interferometry

Guibin Zan[1,2,3], David John Vine[2], Wenbing Yun[2], Sylvia Jia Yun Lewis[2], Qiuping Wang[1] and Ge Wang[3]

[1] National Synchrotron Radiation Laboratory, University of Science and Technology of China, Hefei 230029, People's Republic of China
[2] Sigray, Inc. 5750 Imhoff Drive, Concord, CA 94520, United States of America
[3] Department of Biomedical Engineering, Rensselaer Polytechnic Institute, Troy, NY 12180, United States of America

E-mail: zangb@mail.ustc.edu.cn **and** wyun@sigray.com

RECEIVED
10 September 2019

REVISED
11 December 2019

ACCEPTED FOR PUBLICATION
24 December 2019

PUBLISHED
4 February 2020

Keywords: Talbot–Lau grating interferometry, x-ray imaging, phase contrast imaging, micro array anode structured target, x-ray source, Monte Carlo simulation

Abstract

Talbot–Lau interferometry (TLI) provides additional contrast modes for x-ray imaging that are complementary to conventional absorption radiography. TLI is particularly interesting because it is one of the few practical methods for realizing phase contrast with x-rays that is compatible with large-spot high power x-ray sources. A novel micro array anode structured target (MAAST) x-ray source offers several advantages for TLI over the conventional combination of an extended x-ray source coupled with an absorption grating including higher flux and larger field of view, and these advantages become more pronounced for x-ray energies in excess of 30 keV. A Monte Carlo simulation was performed to determine the optimal parameters for a MAAST source for use with TLI. It was found that the both spatial distribution of x-ray production and the number of x-ray produced in the MAAST have a strong dependence on the incidence angle of the electron beam.

1. Introduction

X-ray mammography, radiology and computed tomography (CT) are among the most widely used diagnostic tools in clinical practice (Russo 2018). Traditionally, these methods depend on differences in x-ray attenuation to generate image contrast. Attenuation contrast is undesirable for imaging living organisms where it is preferable to minimize the dose of ionizing radiation and in the ideal case of no dose the image would have no contrast (Als-Nielsen and McMorrow 2011). X-ray phase contrast imaging (XPCI) is an relatively new method that has been the subject of active development over recent years because phase contrast is much stronger than attenuation contrast for high energy x-ray energies. Since phase contrast by definition does not rely on the absorption of radiation to generate contrast it can have lower dose and therefore is preferable to attenuation contrast for biomedical applications (Taba *et al* 2018, Wilkins *et al* 2014, Bravin *et al* 2013, Lewis 2004). Phase contrast imaging technology generates image contrast based on x-ray phase shift occurring inside the specimen. The strength of attenuation and phase shift is described by the complex refractive index $n = 1 - \delta + i\beta$ where the real part δ describes the phase shift relative to vacuum and the imaginary part β determines the attenuation (Als-Nielsen and McMorrow 2011). The ratio δ/β is greater than 1000 at x-ray energies between 20 and 150 keV for low Z materials which means that XPCI will provide significantly increased contrast for soft tissue specimens (Momose and Fukuda 1995). Another potential advantage of XPCI for soft tissue imaging is inspired by the fact that δ decreases much slower with increasing x-ray energy than β ($1/E^2$, as compared to $1/E^4$ in the regime dominated by photoelectric absorption) (Wilkins *et al* 2014). Therefore, this allows to theoretically reduce the patient dose by obtaining refraction contrast at higher x-ray energies where soft tissue has minimal energy absorption (Zhao *et al* 2012).

The Talbot–Lau interferometry (TLI) is the most promising scheme for translating XPCI into practice due to its compatibility with high power laboratory-based x-ray sources and detectors (Pfeiffer *et al* 2006). It provides attenuation, refraction, and scatter contrast (referred to as tri-contrast) images that could enable better detection of various cancerous tissues beyond the current state of the art x-ray imaging based solely on attenuation contrast

(Pfeiffer *et al* 2008). More recently, scatter (or dark-field) contrast that originates from the small angle scattering of x-rays by fine features has been shown to provide important morphological information from features smaller than the image resolution (Yashiro *et al* 2010, Bech *et al* 2010, Michel *et al* 2013). Among many applications from early-stage osteoarthritis (Stutman *et al* 2011) and breast cancer diagnosis (Taba *et al* 2018, Willner *et al* 2014, Wang *et al* 2014) to lung pathology (Gradl *et al* 2019, Scherer *et al* 2017, Meinel *et al* 2014, Yaroshenko *et al* 2013) envisioned for tri-contrast imaging, the two applications with the highest potential and the largest impact are the diagnosis and monitoring of breast cancer, which ranks as the second most common cancer and the fifth cause of death from cancer across the world (Li *et al* 2018), as well as chronic obstructive pulmonary disease and lung cancer, which are one of the top ten causes of death globally (Gradl *et al* 2019).

A major advantage of TLI is the ability to use a high power x-ray source to perform XPCI with high throughput (Pfeiffer *et al* 2006). However, the introduction of an absorption grating (G0) near the source to enhance the spatial coherence reduces by 50% or more the available photon flux. Additionally, the widespread use of a second absorption, or analyzer grating (G2) to avoid the problem of insufficient resolution of the detector attenuates more than half of the information-carrying x-rays, which consequently doubles the radiation dose compared to a G2-less setup with the same total detected a number of photons. Moreover, multiple measurements (minimum three and typically four to eight) are required to reconstruct tri-contrast images. It not only increases imaging time and dose but also becomes cumbersome for tomography for which multiple images must be acquired for each projection angle (Wang *et al* 2013). Most importantly the challenges of fabricating high aspect ratio absorption gratings are considerable. An absorption grating with 95% opacity of 60 keV x-rays requires $\sim$350 μm thickness of gold which for a modest 3-micron period results in an aspect ratio of greater than 100 : 1 (Thüring *et al* 2014). Additionally, a G0 with large aspect ratio collimates the beam, significantly diminishing the field of view (Thüring *et al* 2011). Even though tiled and bent gratings can be adopted to create large area gratings, the high aspect ratio tiled grating are more difficult to fabricate (Thüring *et al* 2011, Schröter *et al* 2017). Hence, it is highly desirable to develop a single-shot tri-contrast imaging system with a throughput comparable to or considerably better than the existing clinical x-ray imaging systems.

Here we propose an illumination system for TLI which uses a micro array anode structured target (MAAST) that is not subject to the limitations of the extended source and G0 grating combination. The MAAST x-ray source comprises an anode composed of microstructure metal inserts (MMI) in diamond that act x-ray emitters to produce a periodic array of micron sized sub-sources without the use of an absorption grating. A compact TLI with a single transmission grating imaging system combined with a MAAST source has been developed in the laboratory (Morimoto *et al* 2014, 2015a, Morimoto *et al* 2015b). However, the working energy (20 kV) and power loading (60 W) were not optimized to image a large sample quickly. In this work we utilize a commercially available 400 W MAAST x-ray source (Sigray, MAAST-400) (Yun *et al* 2015, Zan *et al* 2019).

In this paper, the properties of MAAST x-ray sources relevant to TLI were studied using a Monte Carlo(MC) simulation. The source was optimized with respect to a range of parameters including incident electron energy, electron beams incidence angle on the MAAST target, and geometric and material parameters of the MAAST. The properties include the spatial distribution of x-rays generated in the tungsten microstructured metal inserts(W-MMI) and the substrate, their relative x-ray production efficiency, and x-ray spectrums. In particular, the dependence of these properties on the electron incidence angle was found to have a significant impact on achieving the highest x-ray generation efficiency.

2. Model and simulations

A MAAST consists of arrays of metal (e.g. Cu, W, Mo) microstructures as x-ray emitters embedded in a diamond substrate, as shown in figures 1(a)–(c). When bombarded with electrons the diamond substrate has several properties that minimize x-ray production relative to the metal microstructures including low mass density, and low atomic number in addition to its outstanding thermal properties that allow it to dissipate heat from the incident electrons more efficiently than any other material. The novel x-ray source has the following advantages. (1) It acts as an array of micron-sized x-ray sources which eliminates the need of the source grating (G0) and all of the associated problems previously described. (2) The electron energy deposition rate in a material is proportional to its mass density, and the x-ray production efficiency in a material by electron bombardment is proportional to its atomic number (Goldstein *et al* 2003). The large ratios of mass density and atomic number between tungsten(W) and diamond result in a favorable spatial x-ray production profile. With the optimized design described in this manuscript up to 98% of x-rays are produced in the tungsten microstructures with only 2% emission from the diamond, forming the equivalent of an almost perfect G0 grating. In other words, this source has high potential to improve contrast further than previous TLI implementations at high x-ray energies that used an extended source and G0 grating. (3) Diamond has the higher thermal conductivity (2200 W mK^{-1}) among the well-known materials (Kandlakunta *et al* 2019, Kidalov and Shakhov 2009). The superior thermal conductivity property is exploited by integrating tungsten structures into diamond with its outstanding thermal

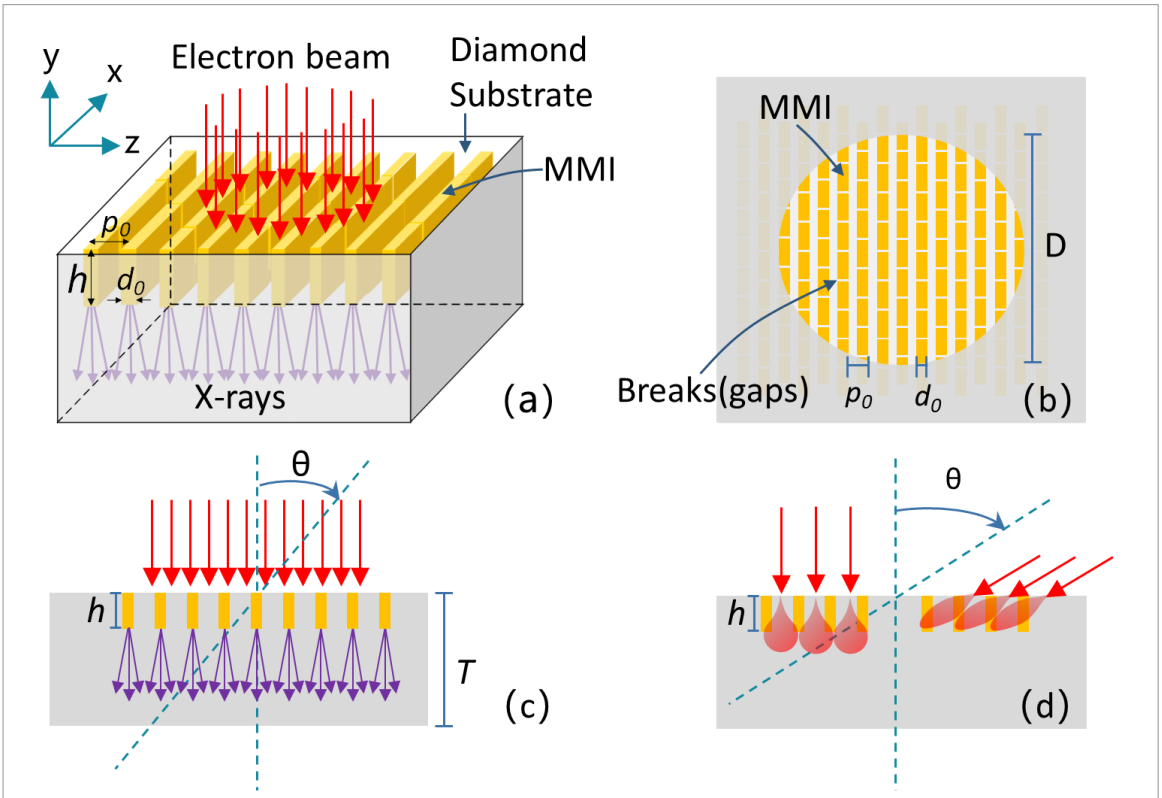

Figure 1. MAAST structure. (a) Perspective, (b) top-down, and (c) front views of a MAAST that comprises a periodic linear array of fine W structures (marked in yellow color) embedded in a diamond substrate. (d) Schematic illustration of electron beam interaction volume inside the MAAST. The breaks in the fine W lines are designed mostly for mechanical and reliability reasons (e.g. to reduce thermal stress).

conductivity (12.7X that of bulk tungsten at room temperature and more than 3.8X that of bulk tungsten at 1000 °C. (4) As a result of the tungsten microstructures have a much higher mass density than the surrounding diamond, the electron energy is preferentially deposited in the microstructures. The microstructures will be heated but the diamond will remain cooler resulting in large thermal gradients that passively cool the microstructures. (5) The fabrication of a high contrast MAAST x-ray source is made much simpler than that of fabricating a high contrast G0 because of the much stronger interaction of electrons with matter compared to x-rays, especially for high energy x-rays.

In order to maximize the x-ray production efficiency in the W-MMIs, the Monte Carlo simulations using Geant4 were used for calculating the electron energy deposition, relative x-ray production efficiency between diamond substrate and MMIs, spatial distribution and x-ray spectrum produced in the MAAST. The recommended energy applicability limit for photons and electrons can be down to 250 eV in Livermore physics List, but can be used down to 10 eV with reduced accuracy (Agostinelli *et al* 2003, Sakata *et al* 2016, Sotiropoulos *et al* 2017, Sakata *et al* 2018). The Geant4 simulation results of energy deposited by the impact of electrons have been shown to be consistent with experimental data over a wide electron beam energy range from a few tens of keV to 1 MeV for various materials and incidence angles. Because the simulation on electron energy deposition profiles using Livermore electromagnetic models based on the EEDL and EPDL data libraries provides good match with experimental results (Batič *et al* 2013, Lechner *et al* 2009), the Livermore physical process model was used in our simulation to calculate the energy deposition in MAAST. The simulation include electron interaction with matter via multiple scattering, ionization, and bremsstrahlung, and photon interaction with matter via Rayleigh scattering, Compton scattering, and photoelectric absorption. X-ray fluorescence and Auger electron emission were also included for the relaxation process of excited atoms. In order to make sure the our Geant4 model is correct and accurate and therefore will produce correct and accurate prediction to optimize MAAST, we compared the predictions of our model to published results, both simulated and experimental, for well-known parameters such as electron backscatter percentage (Ali and Rogers 2008) and energy deposition (Batič *et al* 2013, Lechner *et al* 2009). The consistency between our Geant4 model and the published results have been confirmed.

The simulation model of MAAST is schematically illustrated in figure 1(a). A monoenergetic electron beam with a given energy and incidence angle hits a MAAST with different W-MMI geometric parameters that are summarized in table 1. Three electron energies are considered, 30, 60, and 90 keV. The duty cycle of W-MMI is defined as the ratio of tungsten width (d_0) to MMI structure period (p_0), namely, $\gamma = d_0/p_0$. The depth (h) of

Table 1. The parameters of W-MMIs used in the MC simulation for three x-ray energies for multiple electron incidence angles.

Energy(E)	Geometric parameters of W-MMIs	Incidence angle (degree)
30 keV	$p_0 = 3.0\ \mu$m, $d_0 = 1.0\ \mu$m, $\gamma = 0.33$, $h = 2.16\ \mu$m	0, 30, 45, 60, 80
60 keV	$p_0 = 3.0\ \mu$m, $d_0 = 1.0\ \mu$m, $\gamma = 0.33$, $h = 6.71\ \mu$m	
	$p_0 = 3.0\ \mu$m, $d_0 = 1.5\ \mu$m, $\gamma = 0.50$, $h = 6.71\ \mu$m	
	$p_0 = 2.0\ \mu$m, $d_0 = 1.0\ \mu$m, $\gamma = 0.50$, $h = 6.71\ \mu$m	
90 keV	$p_0 = 3.0\ \mu$m, $d_0 = 1.0\ \mu$m, $\gamma = 0.33$, $h = 12.98\ \mu$m	

W-MMIs along the surface normal was optimized using continuous-slowing-down approximation (CSDA) to estimate the maximum travel range of the electrons in the matter (Berger 2005).

Note that fabricating a MAAST is much easier that a G0 absorption grating because the CSDA is much smaller than the comparable thickness of the gold G0 grating lines required to absorb 95% of x-rays. For example, CSDA value of 12.98 μm for 90 keV electrons (corresponding about 60 keV x-rays used for measurement) is substantially smaller than 350 μm Au required to absorb 95% of x-rays of 60 keV. The substantially smaller CSDA value also means that fabrication of MAAST with small period is feasible, which is important to achieve single-shot tri-contrast imaging combined with an inverse Talbot configuration or Lau effect (Donath *et al* 2009, Momose *et al* 2011). A 1 mm thickness diamond substrate (T) was selected to maximize mechanical strength, thermal dissipation, and x-ray transmission. The incident electron beam profile set to be a uniform 100 μm diameter (D) circle at an incidence angle with respect to the surface normal of the MAAST, as shown in figures 1(c) and (d).

The incidence angle of the electron beam, figure 1(d), and the geometric parameters of the MAAST, such as the duty cycle of W-MMI and size of MMIs, have significant effect on the x-ray production efficiency in the W-MMIs and spatial distribution of the x-rays produced in the MAAST. As shown in figure 1(d), compared with 0-degree incidence angle, an electron impacting the MAAST with a large incidence angle has a greater likelihood of interacting with W-MMIs. For each of the three incident electron energies, five incidence angles were simulated. A total of 20 million primary electrons were simulated for each run which is large enough to ensure that the statistical uncertainties are less than 0.2% (Batič *et al* 2013, Lechner *et al* 2009). The statistical uncertainties of the simulated data were done by calculating the standard error of three times of simulations. They are negligible with a value of less than 0.2%, so the error bars were not plotted in the figures. To save computing time, the production threshold which limits the production of secondary photons and electrons was set to 100 nm.

3. Results and analysis

3.1. Energy deposition in MAAST

As primary electrons impinge on a MAAST a certain fraction will penetrate the surface, and the remainder will be backscattered. The electrons that penetrate into the MAAST convert most of their energy to heat and only a small fraction of the energy is converted to x-rays. The rate of bremsstrahlung production can be described with mass radiation stopping power S_{rad} (in MeV cm^2 g^{-1}) (Podgoršak 2010)

$$S_{rad} = \alpha B_{rad} r_e^2 Z^2 \frac{N_A}{A} E_e \tag{1}$$

where α denotes the fine structure constant, B_{rad} is equal to 16/3 for electron in the non-relativistic energy range, r_e the classical electron radius, Z the atomic number of the target material, N_A the Avogadro constant, A the atomic mass number, E_e the initial total energy of the incident electron. Due to the relationship of $Z/A \approx 0.5$ for all elements with the exception of hydrogen, the rate of bremsstrahlung production is proportional to Z.

The number of backscattered electrons n_{bse} is given by

$$n_{bse} = n \times \eta \tag{2}$$

where n is the number of incident electrons, η is the backscatter coefficient which has a strong dependence on incidence angle θ and atomic number Z (Goldstein *et al* 2003),

$$\eta\,(Z, \theta) = (1 + \cos\theta)^{-9/\sqrt{Z}}. \tag{3}$$

The backscatter coefficient increases rapidly with the incidence angle and depends strongly on the atomic number. The backscatter coefficient of W is about ten times larger than diamond at zero-degree incidence angle, due to the large difference in atomic number Z. The backscatter coefficient only weakly depends on the primary electron energy over the energy range relevant for medical imaging. For example, there is less than 4% backscatter in the energy range of 10–100 keV for tungsten (Behling 2015). The mean energy of the backscattered electrons is slightly smaller than the energy of primary incident electrons. Therefore, the electron incidence angle needs to

be considered when calculating the electron energy deposition and associated x-ray production. This simulation includes the angular dependence of backscatter processes.

To calculate the electron energy deposited in a MAAST a number of numerical simulations were performed using the material and geometric parameters listed in table 1. In particular, it was found that the electron incidence angle on the MAAST (figure 1(d)) is an important parameter in the simulation.

Figures 2–4(a) show the calculated energy deposition in the MAAST target, W-MMIs, and diamond substrate at the five marked electron incidence angles for 30, 60, and 90 keV incident electron energies, respectively. The integrated incident electron energies for 30, 60, and 90 keV are 6.0×10^5 MeV, 1.2×10^6 MeV, and 1.8×10^6 MeV, respectively. The values of the curves from 0-degree to 80-degree in figures 2–4 is obtained by using the B-Spline interpolation of the simulated results at the five incidence angles. Note that the total energy deposition in the MAAST decreases with increasing incidence angle due to the increase of the backscatter coefficient with the incidence angle.

In an ideal MAAST source 100% of the electron energy deposited in the W-MMIs and no energy is deposited in the diamond substrate. We simulated the percentages of the total electron energy deposited in the MAAST in the W-MMIs and the diamond substrate as a function of the incidence angle for 30, 60, and 90 keV electron energies, and the results are shown in figures 2–4(b). The results show that the percentage in the W-MMIs increases with increasing incidence angle while the percentage in the diamond substrate decreases. For a given incident electron energy, the energies deposited in the W-MMIs versus the diamond substrate are equal at a certain incidence angle. This incidence angle for the MAAST with the parameters listed in the table 1 is 46°, 20°, and 8° at 30, 60, and 90 keV electron energies, respectively. For TLI it is preferable to maximize x-ray production in the MMIs and minimize it in the diamond substrate. As the electron energy deposition directly leads to x-rays production, the relative increase of the x-rays produced in the W-MMIs with respect to the x-rays produced in the diamond is favored for TLI. From the thermal performance perspective, the relative temperature increase of the W-MMIs with respect to the diamond substrate leads to larger local thermal gradient for the W-MMIs with increasing incidence angle. The larger local thermal gradient enables higher electron power loading of the MAAST with higher source brightness. However, the incidence angle needs to be considered with practical design of a MAAST source.

The size and the duty cycle of W-MMI in a MAAST directly affects the ratio of energy deposited in the W-MMIs to the diamond substrate. Simulations for 60 keV incident electron energy were performed for: (1) $p_0 = 2.0\ \mu\text{m}, d_0 = 1.0\ \mu\text{m}, \gamma = 0.50, h = 6.71\ \mu\text{m}$; (2) $p_0 = 3.0\ \mu\text{m}, d_0 = 1.5\ \mu\text{m}, \gamma = 0.50, h = 6.71\ \mu\text{m}$.

Figures 5 and 6 present the energy deposition in the MAAST, W-MMIs, and diamond substrate as a function of incidence angle. They present the effect of different period(size) of W-MMIs on the ratio of energy deposition. Note that the energy deposited in the W-MMIs is always bigger than in diamond substrate over range of incidence angles considered with the duty cycle of 0.5. Compared figures 6 with 3, the percentage of energy deposited in W-MMIs with 0.5 duty cycle is also larger than that for 0.33 duty cycle with same period of 3.0 μm. It should be noted that when using a MAAST source for TLI imaging the duty cycle of MMI needs to be smaller than 0.50 to obtain sufficiently high visibility of Talbot interference fringes (Wang *et al* 2010). The etch process of the diamond substrate has a little bit of effect on the duty cycle. Therefore, the duty cycle of 0.33 is preferred for achieving high spatial coherence in our application.

The rate of energy loss with distance traveled is proportional to the atomic number and mass density (Goldstein *et al* 2003). In order to compare the energy deposition between the W-MAAST and bulk diamond and bulk W, the energy deposition coefficient (EDC) was calculated. The EDC is defined as the ratio of deposited to incident energy. Figure 7 shows the EDC of bulk W, bulk diamond and W-MAAST. Bulk W and bulk diamond mean a homogeneous W or diamond target without any structure. The length, width, and height of bulk W and diamond are 10X CSDA which are large enough to ensure the electron has negligible probability of escaping the cubic target. As shown in figure 7, the EDC of W-MAAST is higher than the bulk W and lower than bulk diamond due to the effective atomic number and the mass density of W-MAAST that is due to the structured design. Moreover, the EDC of W-MAAST also presents an strong dependence on the electron energy, especially for larger incident angle. In contrast, the EDCs of bulk diamond and the W show a little bittle dependency on the electron energy.

3.2. Spatial distribution of energy deposited in a MAAST

In order to investigate the spatial distribution of energy deposited in a W-MAAST, the integrated energy deposition of top view (Z-X plane) and cross-sectional plane (Z-Y plane) were calculated. Figure 8 shows the calculated spatial distribution of energy deposited in the Z-X and Z-Y planes. The period of the microstructures is 3.0 μm and the duty cycle is 0.33 giving 1.0-micron width tungsten lines separated by 2.0-microns of diamond. The energy of the incident electron beam is 60 keV and its diameter is 100 μm. The incident angle is 60-degree. The lateral extent of the energy deposition is slightly larger than 100 μm because electrons scatter a small distance outside the electron beam footprint. It is clear to see the differences in spatial distribution of energy deposited

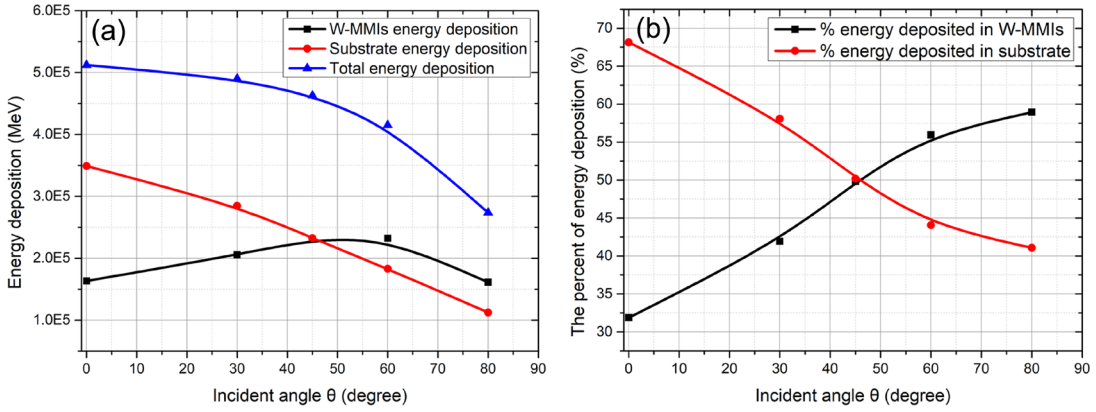

Figure 2. Calculated energy deposition in MAAST, W-MMIs, and diamond substrate (a) and the percentages of energy deposited in W-MMIs and substrate (b). The parameters used for the calculations are: $E = 30$ keV, $p_0 = 3.0$ μm, $d_0 = 1.0$ μm.

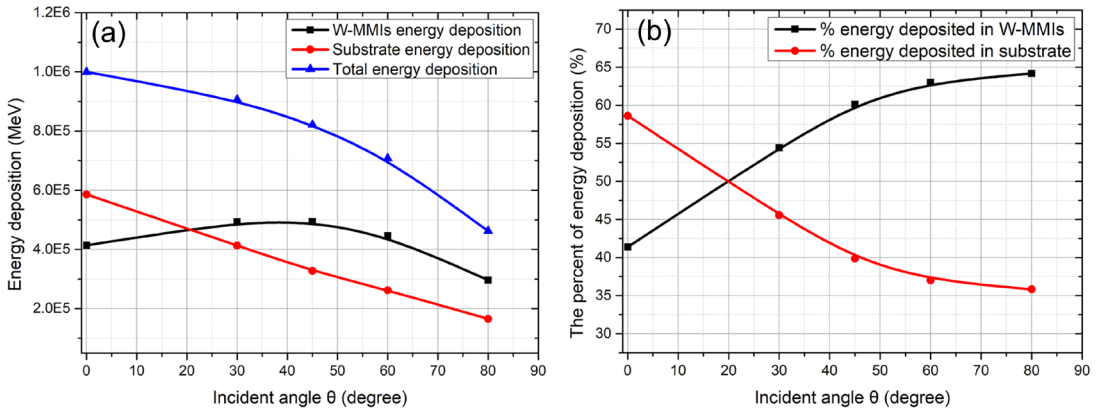

Figure 3. Calculated energy deposition in MAAST, W-MMIs, and diamond substrate (a) and the percentages of energy deposited in W-MMIs and substrate (b). The parameters used for the calculations are: $E = 60$ keV, $p_0 = 3.0$ μm, $d_0 = 1.0$ μm.

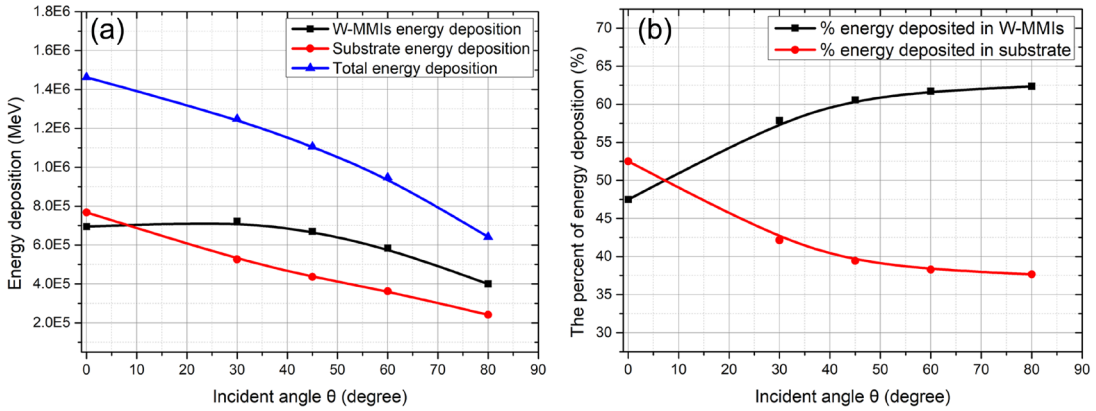

Figure 4. Calculated energy deposition in MAAST, W-MMIs, and diamond substrate (a) and the percentages of energy deposited in W-MMIs and substrate (b). The parameters used for the calculations are: $E = 90$ keV, $p_0 = 3.0$ μm, $d_0 = 1.0$ μm.

between the W-MMIs and diamond substrate. A majority of energy deposited in the W-MMIs due to the atomic number of W is 12.3X larger than diamond, and the mass density of W is 5.5X larger than diamond.

3.3. Relative x-ray production efficiency

In an ideal MAAST source for TLI application all x-rays should be generated in the MMIs and none should be generated in the substrate. A figure of merit of a MAAST source for TLI application is the relative x-ray production efficiency, i.e. the ratio of the x-rays produced in the W-MMIs to the x-rays produced in the diamond

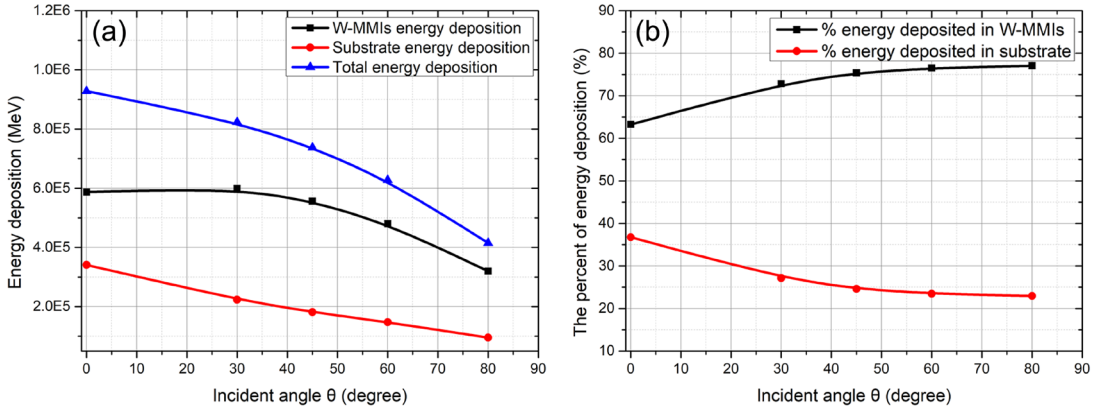

Figure 5. Calculated energy deposition in MAAST, W-MMIs, and diamond substrate (a) and the percentages of energy deposited in W-MMIs and substrate (b). The parameters used for the calculations are: $E = 60$ keV, $p_0 = 2.0$ μm, $d_0 = 1.0$ μm.

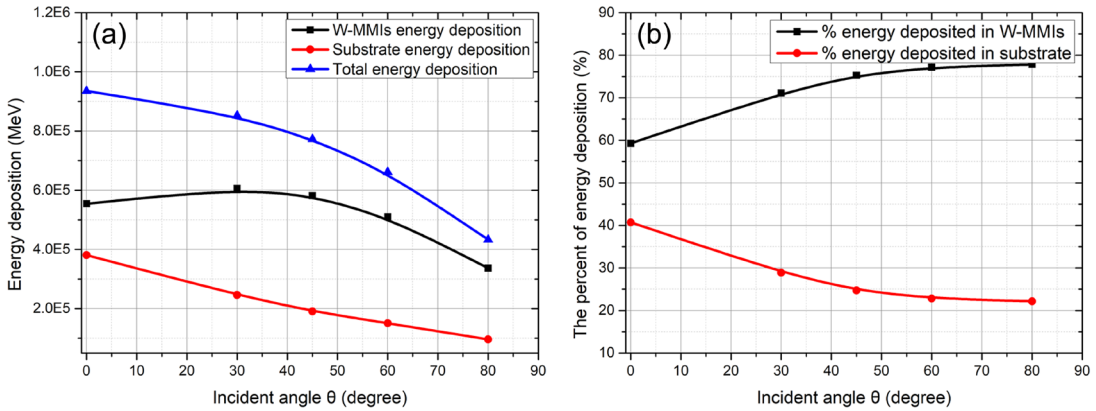

Figure 6. Calculated energy deposition in MAAST, W-MMIs, and diamond substrate (a) and the percentages of energy deposited in W-MMIs and substrate (b). The parameters used for the calculations are: $E = 60$ keV, $p_0 = 3.0$ μm, $d_0 = 1.5$ μm.

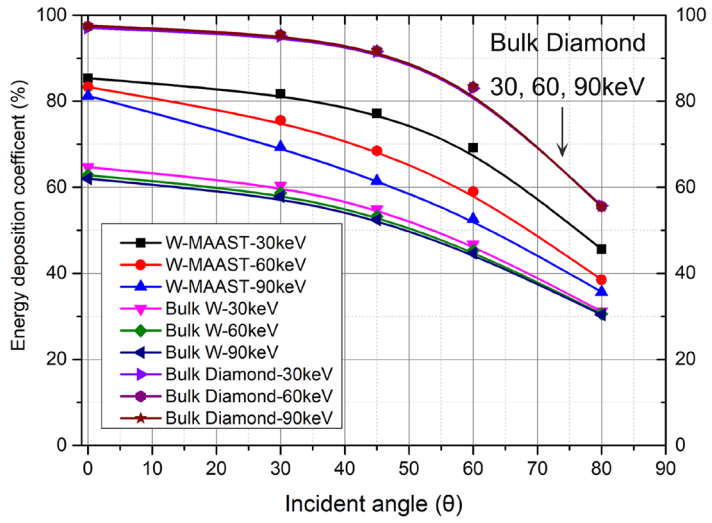

Figure 7. Energy deposition coefficient as a function of electron incident angle. The parameters used for calculation of W-MAAST are: $E = 30, 60,$ and 90 keV, $p_0 = 3.0$ μm, $d_0 = 1.0$ μm.

substrate. Since the rate of bremsstrahlung production is proportional to Z, the relative x-ray production ratio can be approximated,

$$\eta_x = \frac{P_{MMI} \times Z_W}{P_{substrate} \times Z_C} \tag{4}$$

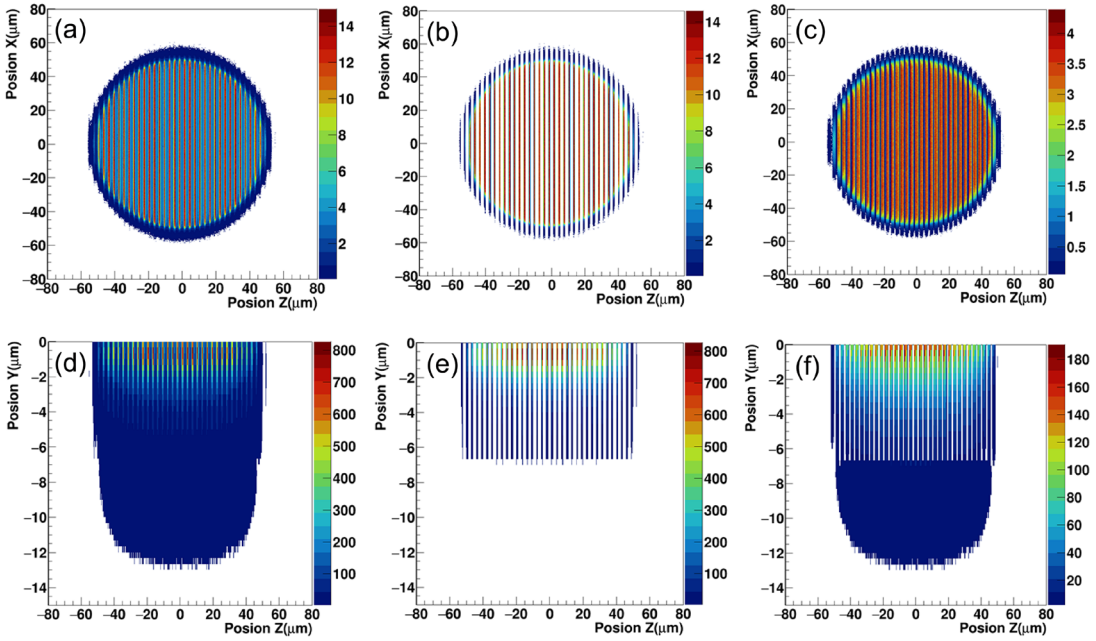

Figure 8. Calculated spatial distribution of energy deposited in the model W-MAAST. (a)–(c) represent spatial distribution on the surface of the W-MAAST target (Z-X plane); (d)–(f) represent spatial distribution of energy deposited in the model W-MAAST on a cross sectional plane (Z-Y plane); (a) and (d) are for total energy deposited in the W-MAAST; (b) and (e) are for energy deposited in the W-MMIs; (c) and (f) are for energy deposited in the diamond substrate.

where P_{MMI} is the percent of energy deposition in W-MMIs, $P_{substrate}$ the percent of energy deposition in the diamond substrate, Z_W is the atomic number of tungsten, and Z_C is the atomic number of the diamond. Figure 9 shows the calculated ratio of the x-rays produced in W-MMIs to the diamond substrate as a function of the incidence angle for the electron energy 30, 60, and 90 keV. Note that for the three incident electron energies, the ratio increases with increasing incidence angle. At 60-degree incidence angle, the increase in the ratio is about 2.7X, 2.4X, 1.8X higher than that at zero- degree incidence angle for the 30, 60, and 90 keV electron energy, respectively.

3.4. Spatial distribution of x-rays produced in a MAAST

The spatial distribution of the x-rays generated in the MAAST target is an important parameter for TLI application. Figure 10 shows the calculated spatial distribution of x-rays produced in the MAAST for three incident angles and 60 keV incident electron energy with 10^{10} primary electrons per simulation. The percentage of the x-rays generated by the W-MMI to the total x-rays generated in the MAAST is given by,

$$R = \frac{I_{W\text{-}MMI}}{I_{W\text{-}MMI} + I_{Diamond}} \times 100\% \tag{5}$$

where $I_{W\text{-}MMI}$ is the total x-rays produced in W-MMI in one period, $I_{Diamond}$ is the total x-rays produced in the diamond in one period. It should be noted that low energy x-rays are more likely to be absorbed by the MAAST so an energy filter was applied to exclude x-rays with energy less than 20 keV. Our simulation produced 91.1%, 96.5%, 97.1% with 0°, 45°, and 60° electron incidence angle at the electron energy of 60 keV, respectively. In order to achieve high sensitivity in Talbot–Lau interferometry, the contrast of the MAAST is the key to get high visibility of interference pattern for increasing the sensitivity (Pfeiffer *et al* 2006, Thüring and Stampanoni 2014). The contrast of W-MAAST is given by,

$$C = \frac{R_{W\text{-}MMI} - R_{Diamond}}{R_{W\text{-}MMI} + R_{Diamond}} \times 100\% \tag{6}$$

where $R_{W\text{-}MMI}$ is the percentage of the x-rays generated by the W-MMI to the total x-rays generated in the W-MAAST, $R_{Diamond}$ is the percentage of the x-rays generated by the W-MMI to the total x-rays generated in the MAAST. The contrasts are 82.2%, 93.0%, 94.2% with 0°, 45°, and 60° electron incidence angle for the electron energy of 60 keV, respectively. Compared to the incidence angle of zero-degree, we estimate that the imaging speed can be improved by 30% with the incident angle of 60° for the electron energy of 60 keV due to the imaging time is inversely proportional to the second power of contrast. For the electron energy of 30 keV, the gain of imaging speed is close to 40% with the incident angle of 60°. It should be noted that the MAAST source for x-ray grating interferometry is suitable for both low energy and high energy x-ray imaging. Therefore, the electron

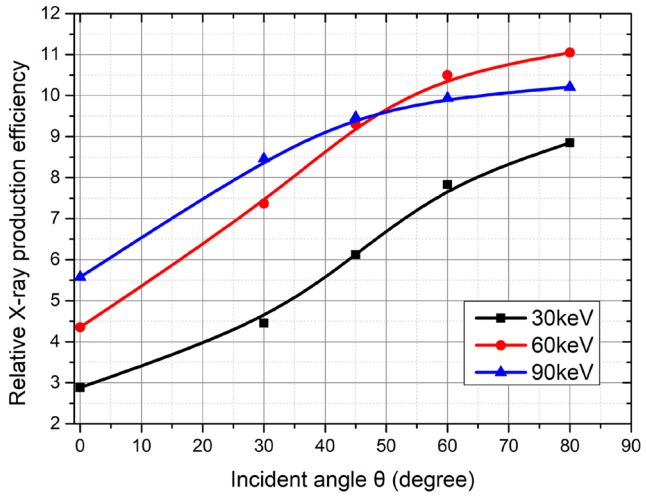

Figure 9. Calculated ratio of x-ray produced in W-MMIs to the x-rays produced in diamond substrate as a function of incidence angle. The parameters used for the calculation are: $E = 30, 60, 90$ keV, $p_0 = 3.0$ μm, $d_0 = 1.0$ μm.

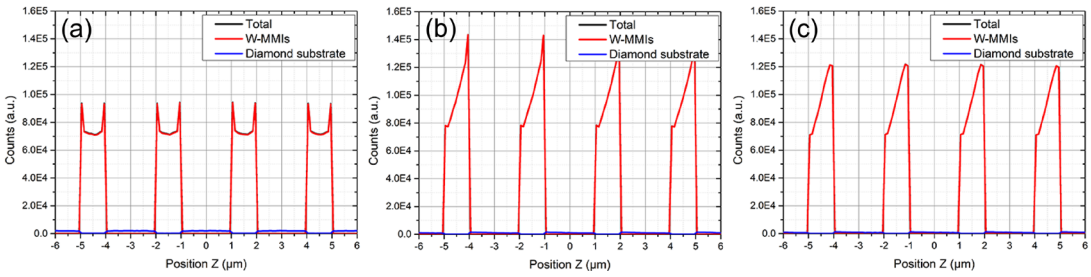

Figure 10. Calculated x-ray spatial distribution of the x-rays produced in W-MMIs (red) and diamond substrate (blue) for three electron beam incidence angles: (a) 0°, (b) 45°, and (c) 60°. The parameters used for the calculations are: $E = 60$ keV, $p_0 = 3.0$ μm, $d_0 = 1.0$ μm.

beam incidence angle should be considered in the practical design with broad application. The large fraction of x-rays produced in the W-MMIs is one of the important advantages of the MAAST x-ray source. This advantage increases with increasing electron incidence angle with respect to the surface normal of the MAAST.

3.5. X-ray spectrum

The grating interferometer can operate over a fairly wide energy bandwidth (Pfeiffer *et al* 2006). However, the x-ray spectrum directly impact the visibility of the interference pattern (Thüring and Stampanoni 2014). Using an energy resolving detector to track the x-ray production position and measure the x-ray energy the spectrum of x-rays produced in a MAAST source is calculated. Figure 11 shows the calculated x-ray spectrum of a W-MAAST as a function of the electron incidence angle at incident electron energy of 60 keV with 10^{10} primary electrons per simulation. The number of x-rays produced in the W-MMIs (red line) is much higher than that produced in diamond substrate (blue line) because Z_W is 12.3 times larger than Z_C. Compared to the incidence angle of zero-degree, 60-degree incidence angle shows more x-rays produced in W-MMIs than the diamond substrate, because more energy deposited in W-MMIs.

4. Discussion

As mentioned previously, the backscattered electrons remove a significant amount of electron energy that would otherwise contribute to x-ray production. The backscatter energy coefficient is used for quantifying the energy taken by the backscatter electrons, which is defined as the percentage of backscatter energy to total incident energy. For this calculation, the electrons backscattered from the W-MAAST are recorded by a detector which is over the W-MAAST surface (Kim *et al* 2015). Figure 12 shows the backscatter coefficient and backscatter energy coefficient as a function of the electron incident angle. The backscatter coefficient is higher than backscatter energy coefficient because electrons lose energy due to inelastic scattering and this energy is transferred to the target atoms before backscattering out. The backscatter coefficient and backscatter energy coefficient of W-MAAST are between bulk tungsten and bulk diamond. For W-MAAST, the backscattered electron takes 40% of input

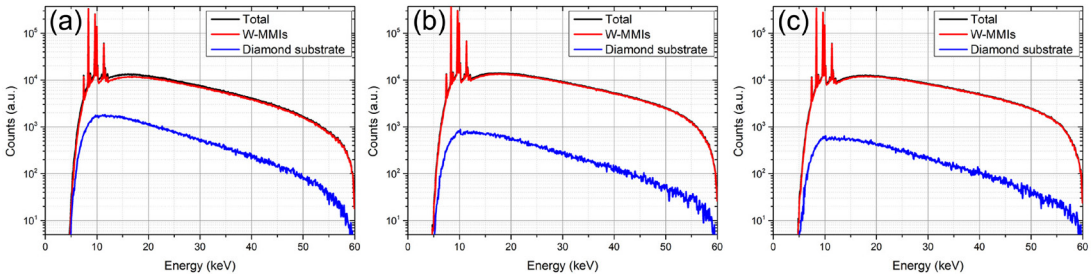

Figure 11. Calculated x-ray spectrum produced in W-MMIs (red) and diamond substrate (blue) for three electron beam incidence angles: (a) 0°, (b) 45°, and (c) 60°. The parameters used for the calculations are: $E = 60$ keV, $p_0 = 3.0$ μm, $d_0 = 1.0$ μm.

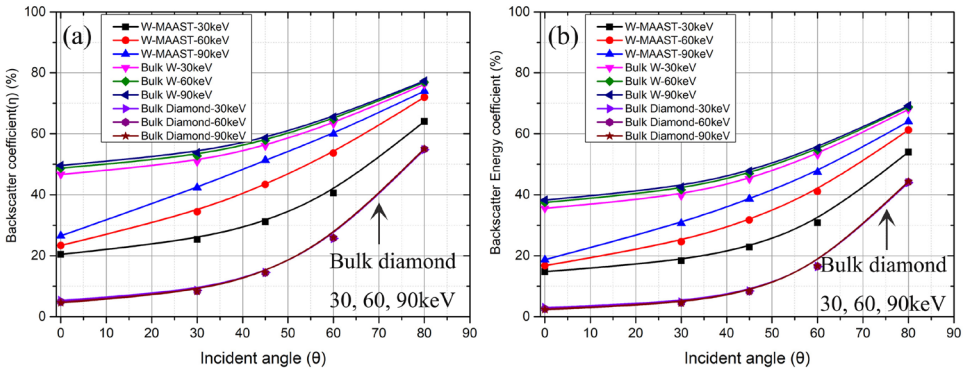

Figure 12. Backscatter coefficient and backscatter energy deposition coefficient as a function of electron incident angle. The parameters used for calculation of W-MAAST are: $E = 30, 60,$ and 90 keV, $p_0 = 3.0$ μm, $d_0 = 1.0$ μm.

energy at the electron energy of 60keV when the electron incident angle is 60-degree. Compared to the 0-degree incident angle, the backscatter coefficient of 60-degree incident angle increases 2.3X, and backscatter energy coefficient increases 2.5X at the electron energy of 60keV. Compared to figure 7, the electron backscattering from the W-MAAST is reasonable to explain the decrease of energy deposition of W-MAAST with large incident angle.

With large electron incident angle, more of the energy is deposited in the MMIs than the diamond substrate which maximizes the ratio of x-rays produced in the MMIs to the diamond substrate. Figure 9 shows that the relative x-ray production efficiency of 60-degree incident angle increases about 2.4X with the same input power loading compared to 0-degree at the electron energy of 60 keV. Therefore, if we use the same power loading as the 0-degree incident angle on the W-MAAST for 60-degree the MMI x-ray flux will be increased.

The MAAST x-ray source replaces the function of the G0 absorption grating and also has many advantages. First, the MAAST source functions well at x-ray energies up to 80 keV x-rays used in diagnostic x-ray imaging equipment because the limited electron penetration distance requires smaller structures that are easier to fabricate than an absorption grating which must be much larger to absorb x-rays that interact much stronger than electrons. Secondly, the FOV can be much larger because the MAAST does not collimate the x-ray beam as a high aspect ratio G0 grating must. Furthermore, Lau effect geometry (Momose *et al* 2011) and Inverse Talbot–Lau geometry (Donath *et al* 2009) are feasible with the MAAST source because small periods can be easily realized which in turn can be used to relax the aspect ratio requirement for G2 absorption grating, meaning that thick structures can be fabricated easily or the G2 can even be removed entirely further simplifying the system.

5. Conclusion

In this work, the MC simulation code Geant4 was used to calculate the properties of the MAAST source that are important for TLI applications, including the spatial distribution of the x-rays generated in the MAAST, percentage of the x-rays generated by the W-MMIs relative to the total x-rays generated in the MAAST, and x-ray spectrum. The input parameters for the simulations include incident electron energy, electron beam incidence angle, and geometric parameters of MAAST. We also simulated the electron backscattering from the W-MAAT to explain the decrement of energy deposition at higher incidence angles. The methodology and the MC simulation results are valuable to guide the design and optimization of MAAST sources. Further work is underway to prototype a MAAST source and experimentally validate our numerical prediction or inform further refinements of the numerical simulation.

Acknowledgment

We would like to express our sincere gratitude to Oliver Diaz from VICOROB research institute, University of Girona for his very useful discussions and suggestions about the Geant4 simulations. This work was partially supported by the National Key Scientific Instrument and Equipment Development Projects of China (CZBZDYZ20140002), the National Institute of Biomedical Imaging and Bioengineering of the National Institutes of Health under award number: R44EB023284.

ORCID iDs

Guibin Zan https://orcid.org/0000-0002-3957-359X

References

Agostinelli S *et al* 2003 GEANT4—a simulation toolkit *Nucl. Instrum. Methods Phys. Res.* A **506** 250–303
Ali E and Rogers D 2008 Benchmarking EGSnrc in the kilovoltage energy range against experimental measurements of charged particle backscatter coefficients *Phys. Med. Biol.* **53** 1527
Als-Nielsen J and McMorrow D 2011 *Elements of Modern X-ray Physics* 2nd edn (New York: Wiley) (https://doi.org/10.1002/9781119998365)
Batič M, Hoff G, Pia M G, Saracco P and Weidenspointner G 2013 Validation of Geant4 simulation of electron energy deposition *IEEE Trans. Nucl. Sci.* **60** 2934–57
Bech M, Bunk O, Donath T, Feidenhans R, David C and Pfeiffer F 2010 Quantitative x-ray dark-field computed tomography *Phys. Med. Biol.* **55** 5529
Behling R 2015 *Modern Diagnostic X-ray Sources: Technology, Manufacturing, Reliability* (Boca Raton, FL: CRC Press) (https://doi.org/10.1201/b18655)
Berger M J 2005 *ESTAR, PSTAR, and ASTAR: Computer Programs for Calculating Stopping-Power and Range Tables for Electrons, Protons, and Helium Ions* (Gaithersburg, MD: NIST) (version 2.0.1) http://physics.nist.gov/star (Accessed: 29 August 2018)
Bravin A, Coan P and Suortti P 2013 X-ray phase-contrast imaging: from pre-clinical applications towards clinics *Phys. Med. Biol.* **58** R1
Donath T *et al* 2009 Inverse geometry for grating-based x-ray phase-contrast imaging *J. Appl. Phys.* **106** 054703
Goldstein J I, Newbury D E, Michael J R, Ritchie N W, Scott J H J and Joy D C 2003 *Scanning Electron Microscopy and X-ray Microanalysis* 3rd edn (New York: Springer) (https://doi.org/10.1007/978-1-4615-0215-9)
Gradl R *et al* 2019 Dynamic *in vivo* chest x-ray dark-field imaging in mice *IEEE Trans. Med. Imaging* **38** 649–56
Kandlakunta P, Thomas A, Tan Y, Khan R and Zhang T 2019 Design and numerical simulations of W-diamond transmission target for distributed x-ray sources *Biomed. Phys. Eng. Express* **5** 025030
Kidalov S and Shakhov F 2009 Thermal conductivity of diamond composites *Materials* **2** 2467–95
Kim S H, Pia M G, Basaglia T, Han M C, Hoff G, Kim C H and Saracco P 2015 Validation test of Geant4 simulation of electron backscattering *IEEE Trans. Nucl. Sci.* **62** 451–79
Lechner A, Pia M G and Sudhakar M 2009 Validation of Geant4 low energy electromagnetic processes against precision measurements of electron energy deposition *IEEE Trans. Nucl. Sci.* **56** 398–416
Lewis R 2004 Medical phase contrast x-ray imaging: current status and future prospects *Phys. Med. Biol.* **49** 3573
Li X, Gao H, Chen Z, Zhang L, Zhu X, Wang S and Peng W 2018 Diagnosis of breast cancer based on microcalcifications using grating-based phase contrast CT *Eur. Radiol.* **28** 3742–50
Meinel F G *et al* 2014 Lung tumors on multimodal radiographs derived from grating-based x-ray imaging–A feasibility study *Phys. Med.* **30** 352–7
Michel T *et al* 2013 On a dark-field signal generated by micrometer-sized calcifications in phase-contrast mammography *Phys. Med. Biol.* **58** 2713
Momose A and Fukuda J 1995 Phase-contrast radiographs of nonstained rat cerebellar specimen *Med. Phys.* **22** 375–9
Momose A, Kuwabara H and Yashiro W 2011 X-ray phase imaging using Lau effect *Appl. Phys. Express* **4** 066603
Morimoto N, Fujino S, Ito Y, Yamazaki A, Sano I, Hosoi T, Watanabe H and Shimura T 2015a Design and demonstration of phase gratings for 2D single grating interferometer *Opt. Express* **23** 29399–412
Morimoto N, Fujino S, Ohshima K I, Harada J, Hosoi T, Watanabe H and Shimura T 2014 X-ray phase contrast imaging by compact Talbot–Lau interferometer with a single transmission grating *Opt. Lett.* **39** 4297–300
Morimoto N, Fujino S, Yamazaki A, Ito Y, Hosoi T, Watanabe H and Shimura T 2015b Two dimensional x-ray phase imaging using single grating interferometer with embedded x-ray targets *Opt. Express* **23** 16582–8
Pfeiffer F, Bech M, Bunk O, Kraft P, Eikenberry E F, Brönnimann C, Grünzweig C and David C 2008 Hard x-ray dark-field imaging using a grating interferometer *Nat. Mater.* **7** 134
Pfeiffer F, Weitkamp T, Bunk O and David C 2006 Phase retrieval and differential phase-contrast imaging with low-brilliance x-ray sources *Nat. Phys.* **2** 258
Podgoršak E B 2010 *Radiation Physics for Medical Physicists* 2nd edn (New York: Springer) (https://doi.org/10.1007/978-3-642-008745-7)
Russo P 2017 *Handbook of X-ray Imaging: Physics and Technology* (Boca Raton, FL: CRC Press) (https://doi.org/10.1201/9781351228251)
Sakata D *et al* 2016 An implementation of discrete electron transport models for gold in the Geant4 simulation toolkit *J. Appl. Phys.* **120** 244901
Sakata D *et al* 2018 Geant4-DNA track-structure simulations for gold nanoparticles: the importance of electron discrete models in nanometer volumes *Med. Phys.* **45** 2230–42
Scherer K *et al* 2017 X-ray dark-field radiography *in vivo* diagnosis of lung cancer in mice *Sci. Rep.* **7** 402
Schröter T J *et al* 2017 Large-area full field x-ray differential phase-contrast imaging using 2D tiled gratings *J. Phys. D: Appl. Phys.* **50** 225401
Sotiropoulos M, Taylor M, Henthorn N, Warmenhoven J, Mackay R, Kirkby K and Merchant M 2017 Geant4 interaction model comparison for dose deposition from gold nanoparticles under proton irradiation *Biomed. Phys. Eng. Express* **3** 025025

Stutman D, Beck T J, Carrino J A and Bingham C O 2011 Talbot phase-contrast x-ray imaging for the small joints of the hand *Phys. Med. Biol.* **56** 5697

Taba S T, Gureyev T E, Alakhras M, Lewis S, Lockie D and Brennan P C 2018 X-ray phase-contrast technology in breast imaging: principles, options, and clinical application *AJR. Am. J. Roentgenol.* **211** 133–45

Thüring T, Abis M, Wang Z, David C and Stampanoni M 2014 X-ray phase-contrast imaging at 100 keV on a conventional source *Sci. Rep.* **4** 5198

Thüring T and Stampanoni M 2014 Performance and optimization of x-ray grating interferometry *Phil. Trans. R. Soc.* A **372** 20130027

Thüring T, Modregger P, Grund T, Kenntner J, David C and Stampanoni M 2011 High resolution, large field of view x-ray differential phase contrast imaging on a compact setup *Appl. Phys. Lett.* **99** 041111

Wang Z *et al* 2013 X-ray phase radiography and tomography with grating interferometry and the reverse projection technique *J. Phys. D: Appl. Phys.* **46** 494003

Wang Z, Hauser N, Singer G, Trippel M, Kubik-Huch R A, Schneider C W and Stampanoni M 2014 Non-invasive classification of microcalcifications with phase-contrast x-ray mammography *Nat. Commun.* **5** 3797

Wang Z *et al* 2010 Quantitative coherence analysis with an x-ray Talbot–Lau interferometer *Anal. Bioanal. Chem.* **397** 2091–4

Wilkins S, Nesterets Y I, Gureyev T, Mayo S, Pogany A and Stevenson A 2014 On the evolution and relative merits of hard x-ray phase-contrast imaging methods *Phil. Trans. R. Soc.* A **372** 20130021

Willner M *et al* 2014 Quantitative breast tissue characterization using grating-based x-ray phase-contrast imaging *Phys. Med. Biol.* **59** 1557

Yaroshenko A *et al* 2013 Pulmonary emphysema diagnosis with a preclinical small-animal x-ray dark-field scatter-contrast scanner *Radiology* **269** 427–33

Yashiro W, Terui Y, Kawabata K and Momose A 2010 On the origin of visibility contrast in x-ray Talbot interferometry *Opt. Express* **18** 16890–901

Yun W, Lewis S J Y, Kirz J and Lyon A F 2015 X-ray interferometric imaging system *US Patent* US20150117599A1

Zan G, Vine D, Spink R I, Yun W, Wang Q and Wang G 2019 Design optimization of a periodic microstructured array anode for hard x-ray grating interferometry *Phys. Med. Biol.* **64** 145011

Zhao Y *et al* 2012 High-resolution, low-dose phase contrast x-ray tomography for 3D diagnosis of human breast cancers *Proc. Natl Acad. Sci. USA* **109** 18290–4